

Excited State Dynamics of a Conformationally Fluxional Copper Coordination Complex

Bronte J. Charette, Shelby R. King, Jiaqi Chen, Annika R. Holm, Justin T. Malme, Robert D. Cook, Richard D. Schaller, Nicholas E. Jackson, and Lisa Olshansky*



Cite This: <https://doi.org/10.1021/acs.jpca.3c04269>



Read Online

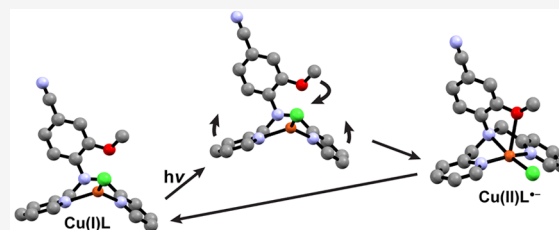
ACCESS |

Metrics & More

Article Recommendations

Supporting Information

ABSTRACT: The conversion of solar energy into chemical fuel represents a capstone goal of the 21st century and has the potential to supply terawatts of power in a globally distributed manner. However, the disparate time scales of photodriven charge separation (\sim fs) and steps in chemical reactions (\sim μ s) represent an inherent bottleneck in solar-to-fuels technology. To address this discrepancy, we are developing earth-abundant coordination complexes that undergo light-induced conformational rearrangements such that charge separation (CS) is hastened, while charge recombination (CR) is slowed. To these ends, we report the preparation and characterization of a new series of conformationally fluxional copper coordination complexes that contain a twisted intramolecular charge transfer (TICT) fluorophore as part of their ligand scaffold. Structural and spectroscopic characterization of the Cu(I) and Cu(II) complexes formed with these ligands in their ground states establish oxidation state-dependent conformational dynamicity, while time-resolved emission and transient absorption spectroscopies define the photophysical parameters of photo-induced excited states. Building on initial reports with a related set of molecules, the improved ligand design presented here greatly simplifies the observed photophysics, effectively shutting down unwanted ligand-centered excited states previously observed. Time-dependent density functional theory (TDDFT) analyses reveal an unusual metal-to-TICT electronic transition only reported once before, and though the formation of a CS state is not observed directly through experiments, TDDFT geometry optimizations in the excited states support the formation of transient Cu(II) CS species, lending credence to the potential success of our approach. These studies establish a clear model for the excited state dynamics at play in proof-of-concept systems and clarify key design parameters for future optimizations toward achieving long-lived CS via photoinduced conformational gating.

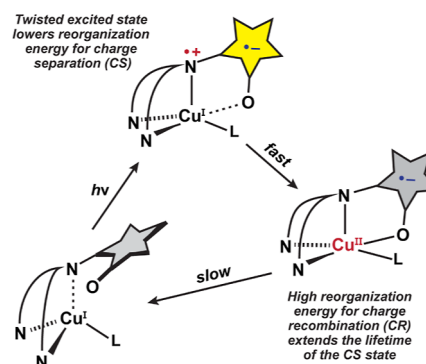


INTRODUCTION

Energy conversion processes in biology often rely on conformational gating mechanisms,^{1,2} where in many cases, such mechanisms enable control over the direction of electron transfer events.^{3,4} Conformational gating operates by linking changes in macroscopic molecular structure to changes in subatomic electronic structure at an embedded cofactor. As we seek to reconstruct our energy infrastructure, a reimagining of our strategies may benefit from the incorporation of such conformational gating mechanisms within synthetic and artificial systems. Herein, we present one strategy to this end, where photo-induced conformational changes in a ligand engender control over the electronic structure of a bound Cu(II/I) ion. Here, we take advantage of the differential oxidation state-dependent coordination properties of Cu(I) and Cu(II). Incorporating a structurally dynamic fluorophore into the ligand architecture provides a means with which to link photo-induced structural changes at the ligand to control over the relative rates of charge separation (CS) and charge recombination (CR) (Scheme 1).

We previously reported the preparation of conformationally dynamic Cu(I),⁵ and Cu(II) complexes.⁶ Incorporation of a

Scheme 1. Strategy Employed to Affect Charge Separation through Conformational Control



Received: June 25, 2023

Revised: July 26, 2023

twisted intramolecular charge transfer (TICT) fluorophore into these dynamic ligands provided the first example of our strategy to employ photo-induced ligand conformational changes in driving fast CS and imposing a large reorganization energy penalty on CR.⁷ This strategy critically relies on the fact that Cu(I) and Cu(II) have different coordination properties; the former tend to adopt linear, trigonal, or tetrahedral geometries and bind to highly polarizable ligands, while the latter are stabilized in tetragonal coordination geometries in the presence of weakly polarizable ligands.⁸ Initial attempts at leveraging these properties to gate photo-induced CS revealed that the desired photophysical processes were dwarfed by the predominance of unwanted ligand-centered transitions. Through ligand modification, we have now solved this challenge and present a clear and cohesive model for the photophysics of these systems as determined by both ground and excited state spectroscopic and computational methods.

METHODS

Materials. Acetonitrile (MeCN), methanol (MeOH), pentane, dimethylformamide (DMF), and dichloromethane (DCM), obtained from Fisher Scientific, were purified further using a Jorg C. Meyer Solvent Purification System in which hydrocarbon and ethereal solvents were sparged with nitrogen before being deoxygenated and dried by passage through Q5 and activated alumina columns, respectively. Anhydrous dimethylacetamide (DMA) was obtained from Sigma-Aldrich and stored over activated sieves. Halogenated solvents were sparged with nitrogen and passed through two activated alumina columns. Water was obtained from an 18 M Ω Milli-Q purification system. CuCl₂·2H₂O was obtained from Fisher Scientific, NH₄PF₆ from Oakwood Chemicals, and all deuterated solvents were from Cambridge Isotope Laboratory. CuCl, obtained from Mallinckrodt, was stirred in acetic acid and subsequently washed with ethanol and diethyl ether before use. Ferrocene (Fc⁰) was purified by recrystallization from hexanes and [Bu₄N]PF₆ (Oakwood Chemicals) was recrystallized three times from ethanol and dried under vacuum. Ligand starting materials dpa^H and dpa^{OMe} were obtained as previously described.^{5,9,10} Here, the abbreviation dpa^R stands for dipicolylamine with the indicated (H or OMe) R-group in the *ortho*-position of the aniline moiety. The abbreviation dpan^R used throughout this report stands for versions of dpa^R that also contain *para*-CN functional groups.

Synthetic Methods. Unless otherwise noted, all manipulations were carried out under N₂ using standard Schlenk line and glovebox techniques.

CuCl(dpan^{OMe}). In a vial equipped with a stir bar in an anaerobic glovebox, CuCl (0.033 g, 0.33 mmol) was dissolved in MeCN (2 mL), to which a solution of dpan^{OMe} (0.11 g, 0.33 mmol) in MeCN (5 mL) was then added, and the solution was stirred for 16 h. Upon completion, the solvent was removed under reduced pressure, and the solid product was further purified by the addition of DCM followed by pentane (4 \times) to obtain the pure product as a yellow solid (0.12 g, 87%). X-ray diffraction (XRD) quality crystals were obtained from the filtrate of the DCM/pentane solution at -36 °C. ¹H NMR (600 MHz, CD₂Cl₂): δ 3.83 (s, 3H), 4.45 (s, 4H), 7.07–7.08 (d, *J* = 6.0 Hz, 2H), 7.16–7.18 (d, *J* = 6.0 Hz, 1H), 7.27–7.32 (m, 4H), 7.73–7.76 (t, *J* = 9.0 Hz, 2H), 8.72–8.73 (d, *J* = 6.0 Hz, 2H). ¹³C{¹H} NMR (600 MHz, DMSO-*d*₆): δ 157.0, 152.2, 149.9, 142.7, 138.5, 125.7, 124.5, 124.2, 120.0, 119.5, 115.5, 105.2, 57.6, 56.8. IR (neat): 2222, 1595, 1258, 1150,

1026, 769 cm⁻¹. HRMS: ESI-positive ion mode *m/z* [M⁺] calcd. for, 428.0465; found, 428.0459. Anal. Calcd (found) for C₂₀H₁₈ClCuN₄O₁·(H₂O)_{0.5} (%): C, 54.80 (55.03); H, 4.37 (4.20); N, 12.78 (12.69).

[CuCl(dpan^{OMe})]PF₆. In air, dpan^{OMe} (0.04 g, 0.12 mmol) was dissolved in MeOH (3 mL). A solution of CuCl₂·2H₂O (0.02 g, 0.13 mmol) in water (3 mL) was added and the reaction was allowed to stir for 4 h. NH₄PF₆ (0.08 g, 0.49 mmol) in water (5 mL) was added to the reaction, and the solution was allowed to stir for an additional 16 h. The resulting precipitate was filtered, washed with water, and dried under reduced pressure to yield a light blue solid (0.04 g, 56%). XRD quality crystals were obtained from vapor diffusion of pentane into acetone at -20 °C. IR (neat): 2237, 1611, 1447, 1287, 1124, 1013, 828, 770 cm⁻¹. HRMS: ESI-positive ion mode *m/z* [M⁺] calcd. for, 428.0465; found, 428.0398. Anal. Calcd (found) for: C₂₀H₁₈ClCuF₆N₄OP: C, 41.82 (41.48); H, 3.16 (3.07); N, 9.75 (9.59).

CuCl(dpan^H). In a vial equipped with a stir bar in an anaerobic glovebox, CuCl (0.033 g, 0.33 mmol) was dissolved in MeCN (2 mL). A solution of dpan^H (0.10 g, 0.33 mmol) in MeCN (5 mL) was then added, and the solution was stirred for 16 h. Upon completion, the solvent was removed under reduced pressure, and the crude solid was purified by the addition of DCM followed by pentane (4 \times) to obtain the pure product as a pale-yellow solid (0.08 g, 64%). ¹H NMR (600 MHz, DMSO-*d*₆): δ 4.91 (s, 4H), 6.74–6.75 (br, 2H), 7.44 (br, 2H), 7.50–7.51 (br, 2H), 7.58 (br, 2H) (br, 2H), 8.60 (br, 2H). ¹³C{¹H} NMR (600 MHz, DMSO-*d*₆): δ 157.6, 152.1, 150.2, 138.8, 133.7, 124.1, 123.5, 120.1, 114.6, 99.6, 58.3. IR (neat): 2214, 1599, 1519, 1398, 1176, 944, 817, 760 cm⁻¹. HRMS: ESI-positive ion mode *m/z* [M⁺] calcd. for, 398.0360; found, 398.0581. Anal. Calcd (found) for C₁₉H₁₆ClCuN₄·H₂O: C, 54.68 (54.87); H, 4.35 (3.95); N, 13.42 (13.17).

CuCl₂(dpan^H). In air, dpan^H (0.08 g, 0.26 mmol) was dissolved in MeOH (1 mL). To this, a solution of CuCl₂·2H₂O (0.05 g, 0.29 mmol) in H₂O (1 mL) was added dropwise. The resulting dark green solution was stirred at room temperature overnight. The product was isolated from these conditions as a green crystalline solid by cooling to -20 °C for two days. IR (neat): 2216, 1599, 1515, 1437, 1178, 820, 760 cm⁻¹. HRMS: ESI-positive ion mode *m/z* [M⁺] calcd. for, 433.0048; found, 433.0105. Anal. Calcd (found) for: C₁₉H₁₆C₁₂CuN₄: C, 52.48 (52.19); H, 3.71 (3.47); N, 12.89 (12.54).

Physical Methods and Instrumentation. ¹H and ¹³C NMR data were collected on Bruker spectrometers operating 600 MHz at ambient temperatures. Chemical shifts are referenced to residual solvent peaks: CDCl₃ (δ 7.26 ppm for ¹H and δ 77.16 for ¹³C), CD₂Cl₂ (δ 5.32 ppm for ¹H and δ 53.84 for ¹³C), and (CD₃)₂SO (δ 2.50 ppm for ¹H and δ 39.52 for ¹³C). Steady-state UV-visible absorption spectra were obtained on an Agilent Technologies 8454 spectrophotometer at ambient temperature. Perpendicular-mode X-band EPR spectra were collected using a Bruker EMX spectrometer equipped with an ER041XG microwave bridge using the following spectrometer settings: attenuation = 20 dB, microwave power = 2.0 mW, frequency = 9.35 GHz, modulation amplitude = 4.0 G, gain = 30 dB, conversion time = 8.01 ms, time constant = 5.12 ms, sweep width = 2500 G and resolution = 5000 points. EPR spectra were modeled using EasySpin/Matlab.¹¹ Fourier-transform infrared (FTIR) spectra were recorded on the JASCO FTIR-6600 Spectrometer using a

Diamond ATR. High-resolution mass spectra were obtained on a Waters Synapt G2-Si electrospray ionization instrument at the UIUC School of Chemical Sciences Mass Spectrometry Laboratory. CHN elemental analysis was conducted on an Exeter Analytical CE 440 instrument in the UIUC School of Chemical Sciences Microanalysis Laboratory.

Steady-state emission spectra were obtained on the Horiba FluoroMax Plus spectrophotometer at ambient temperature. Fluorescence quantum yields were determined relative to 9,10-diphenylanthracene ($\Phi_F = 0.90$ when excited between 275 and 405 nm and collected between 380 and 550 nm in cyclohexane).^{12,13} Solutions of the sample (S) under study were prepared with OD = 0.02, 0.04, 0.06, 0.08, and 0.1 in DCM, while solutions of the reference (R) were prepared 100-fold more dilute in cyclohexane due to its high Φ_F at the excitation wavelength used. The fluorescence spectra of each S and R were measured using the same slit widths and instrument settings across the series. Integrated fluorescence intensity was plotted vs absorbance to obtain the slope of the line as the gradient in eq 1, where subscripts S and R indicate sample or reference, and η is the refractive index of the solvent.

$$\Phi_S = \Phi_R \frac{\text{Gradient}_S \left(\frac{\eta_S}{\eta_R} \right)^2}{\text{Gradient}_R} \quad (1)$$

Electrochemical Methods. Electrochemical experiments were performed on a Pine Wavedriver 10 potentiostat using a 3.0 mm glassy carbon working electrode, a platinum wire auxiliary electrode, and a silver wire pseudo-reference electrode. Data acquisition was carried out at ambient temperature (20–24 °C) in a nitrogen-filled glovebox for solution samples containing 1.0 mM of analyte and 100 mM of $[\text{Bu}_4\text{N}][\text{PF}_6]$ supporting electrolyte dissolved in dry, degassed CH_2Cl_2 . All potentials were referenced to $[\text{Cp}_2\text{Fe}]^{+/0}$ redox couple by adding ferrocene as an internal standard at the end of each experimental run.

Crystallographic Methods. XRD data for all complexes were collected on single crystals mounted on a glass fiber using Paratone oil. Data were acquired with a Bruker D8 Venture kappa diffractometer equipped with a Photon II CPAD detector. An $1\mu\text{s}$ microfocus source provided the Mo K α radiation ($\lambda = 0.71073 \text{ \AA}$) that was monochromated with multilayer mirrors. The collection, cell refinement, and integration of intensity data were carried out using APEX3 software. Multiscan absorption corrections were performed numerically with SADABS. Subsequent calculations were carried out using the SHELXTL program suite.^{14–16} The structures were solved by direct methods and refined on F2 by full-matrix least-squares techniques. Analytical scattering factors for neutral atoms were used throughout the analyses. Hydrogen atoms were generated in calculated positions and refined using a riding model. ORTEP diagrams were generated using ORTEP-3 for Windows.

Time-Resolved Spectroscopy. Transient spectroscopy measurements were carried out using a laser system at Argonne National Laboratory (Spectra Physics, Spitfire, 2 kHz, 35 fs, 800 nm). For transient absorption (TA) measurements, pump and probe beams originated from the same 800 nm pulse. The pump beam was generated using the fourth harmonic output of an optical parametric amplifier (TOPAS, Light Conversion) to create 315 nm photons. The pump is mechanically chopped to 1000 Hz and focused onto the sample plane with a quartz lens. The pump beam size was 300 μm FWHM. Approximately, 5%

of the laser output was split off and focused into a translating CaF_2 crystal to produce a white light supercontinuum. Before generating the probe, the 800 nm beam is double passed into a retroreflecting delay line. This enabled femtosecond stepping and up to 5 ns of delay. After probe generation, the beam is collimated and re-focused onto the sample using reflective optics to limit group velocity dispersion. In the sample plane, the probe beam size is $\sim 50 \mu\text{m}$ FWHM diameter. The transmitted beam is focused into a multimode optical fiber, which couples into a grating spectrograph that disperses the probe wavelengths and reads single laser shots on a CMOS detector (Ultrafast Systems, Helios). Every pump-on (I_p) and pump-off (I_0) probe pulse was measured individually, allowing a shot-to-shot calculation of the transient signal in ΔOD units: $\Delta A(\lambda, t) = \log_{10}(I_0/I_p)$. The experiments were performed in transmission geometry with the sample contained in a 1 mm quartz cuvette. TA measurements were performed on DCM solutions of dpan^{OMe/H} ligands and Cu^I complexes.

Time-resolved photoluminescence (TRPL) spectroscopy was performed using a 35 fs, 2 kHz amplified Ti:sapphire laser (Spectra Physics, Spitfire) that pumped an optical parametric amplifier to produce 315 nm pump pulses in the same manner as for TA. PL was collected with a quartz lens, passed through a long-pass filter, dispersed in a 0.15 m spectrograph, and detected with a single-photon sensitive streak camera detector (Hamamatsu).

Samples for both TA and TRPL were prepared in DCM in an inert atmosphere glovebox. Bulk solutions were prepared to have equivalent optical densities between 0.2 and 0.5 at $\lambda = 315 \text{ nm}$. After both TA and TRPL measurements, samples were assessed for decomposition via steady-state UV–vis absorption spectroscopy. We observed <5% sample decomposition for both $\text{Cu}(I)$ complexes over this time, while ligand decomposition was <10% under the same conditions, as assessed by UV–vis absorption spectroscopy (Table S1). fs TA spectra were corrected for group velocity dispersion using Surface Explorer software (Ultrafast Systems). TRPL kinetics were fit to either a one- or two-component sum of exponentials convoluted with a Gaussian instrument response function. TA kinetics were fit to a three-component sum of exponentials convoluted with a Gaussian instrument response function. The decay kinetics obtained from fitting are provided in the SI.

Computational Methods. Ground-state geometry optimizations were performed at the wB97X-D3/def2-TZVP/SMD(*N,N*-dimethylacetamide) level of theory using default optimization criteria and TightSCF settings. All calculations were performed using Orca.¹⁷ The ten lowest lying vertical singlet and triplet excitation energies were calculated at the optimized ground-state geometries using time-dependent density functional theory (TDDFT) and the Tamm–Dancoff approximation without the use of the resolution-of-the-identity approximation or auxiliary basis sets. Excited state geometry optimizations were then performed following the excitation corresponding to the lowest energy singlet excitation (S_1). Natural transition orbitals (NTO) were computed to image the transition of electron density between ground and various excited states in all relevant geometries.

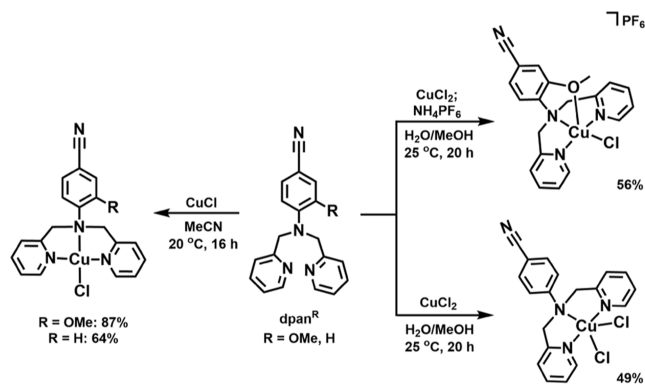
RESULTS

Synthesis and Structural Characterization. Dipicolylamine ligands functionalized with a TICT fluorophore were prepared by a three-step synthetic protocol described in Schemes S1 and S2. Reductive amination of the aryl amine

starting material,^{5,9,10} followed by formylation, and oxidative cyanation, provided dpan^{OMe} and dpan^{H} in 11 and 33% overall yields, respectively. Crystal structures of both dpan^{OMe} and dpan^{H} ligands are presented in Figure S1.

Metallation with CuCl_2 produced $[\text{CuCl}(\text{dpan}^{\text{OMe}})]\text{PF}_6$ and $\text{CuCl}_2(\text{dpan}^{\text{H}})$ according to Scheme 1. Consistent with our previous findings,^{5,7} the presence of the *ortho*-OMe substituent in dpan^{OMe} results in ethereal ligation rather than ligation from a second chloride ligand, as is observed for the metalated product of dpan^{H} (Scheme 2). Dropwise addition of a solution

Scheme 2. Preparation of $\text{CuCl}(\text{dpan}^{\text{OMe}})$, $\text{CuCl}(\text{dpan}^{\text{H}})$, $[\text{CuCl}(\text{dpan}^{\text{OMe}})]\text{PF}_6$, and $\text{CuCl}_2(\text{dpan}^{\text{H}})$



of NH_4PF_6 in MeOH facilitates precipitation of $[\text{CuCl}(\text{dpan}^{\text{OMe}})]\text{PF}_6$, and subsequent vapor diffusion of pentane into acetone at -20 °C provided blue crystals of sufficient quality for XRD. The preparation of crystalline $\text{CuCl}(\text{dpan}^{\text{OMe}})$ was accomplished by the addition of CuCl to dpan^{OMe} in MeCN. The solid-state structures of $\text{CuCl}(\text{dpan}^{\text{OMe}})$ and $[\text{CuCl}(\text{dpan}^{\text{OMe}})]\text{PF}_6$ are shown in Figure 1.

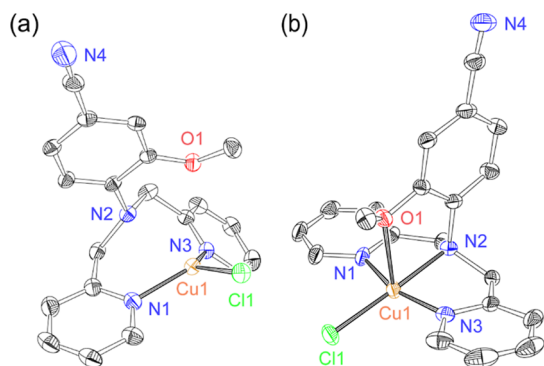


Figure 1. Single-crystal XRD structures of $\text{CuCl}(\text{dpan}^{\text{OMe}})$ (a), and $[\text{CuCl}(\text{dpan}^{\text{OMe}})]^+$ (b) with thermal ellipsoids plotted at 50%. Colors are: orange, green, red, blue, and black for Cu, Cl, O, N, and C, respectively. Co-crystallized solvent molecules, counterions, and H atoms are omitted for clarity.

Similar conditions were used to prepare single crystal samples of $\text{CuCl}_2(\text{dpan}^{\text{H}})$, where dropwise addition of a solution of CuCl_2 in water to dpan^{H} in MeOH and storage of the product at -20 °C provided dark green crystals. X-ray quality yellow crystals of $\text{CuCl}(\text{dpan}^{\text{OMe}})$ were prepared by resuspending crude $\text{CuCl}(\text{dpan}^{\text{OMe}})$ in minimal DCM, followed by precipitation with excess pentane and storage at -36 °C. The solid-state structure of $\text{CuCl}_2(\text{dpan}^{\text{H}})$ is provided in Figure S2.

The XRD structures of $\text{CuCl}(\text{dpan}^{\text{OMe}})$ and $[\text{CuCl}(\text{dpan}^{\text{OMe}})]\text{PF}_6$ presented in Figure 1 highlight the stark contrast between primary coordination spheres operative in the Cu(I) and Cu(II) complexes of dpan^{OMe} . We note that two very similar structures were obtained within the unit cell for $\text{CuCl}(\text{dpan}^{\text{OMe}})$, which are presented in Figure S3 and Table S2. Both are best described as having three-coordinate distorted trigonal planar coordination geometries about the Cu(I) ion and primarily differ in their $\text{Cu}\cdots\text{N}2$ distance, varying from 2.471(2) to 2.527(2) Å (Table S2). The latter structure is featured in Figure 1a. Figure 1b provides the XRD structure of $[\text{CuCl}(\text{dpan}^{\text{OMe}})]\text{PF}_6$, a five-coordinate complex with a τ_5 parameter of 0.20,¹⁸ indicative of a distorted square pyramidal coordination geometry (τ_5 range from 0 to 1 for square pyramidal and trigonal bipyramidal geometries, respectively). The coordinate bond lengths surrounding the Cu(II) ion are all similar to those reported for $[\text{CuCl}(\text{dpaa}^{\text{OMe}})]\text{BPh}_4$ (dpaa^{R} ligands have an acyl rather than nitrile electron-withdrawing group but are otherwise identical).⁷ The τ_5 value for $\text{CuCl}_2(\text{dpan}^{\text{H}})$ not only reflects its trigonal bipyramidal coordination geometry but also reveals a significant lengthening of the $\text{Cu}-\text{N}2$ bond length from 2.068(4) Å for the Cu(II) structure with dpan^{OMe} to 2.292(2) Å for the Cu(II) structure with dpan^{H} (Table 1). Effects of this

Table 1. Select Bond Lengths (Å) in the XRD Structures of $\text{CuCl}(\text{dpan}^{\text{OMe}})$, $[\text{CuCl}(\text{dpan}^{\text{OMe}})]^+$, and $\text{CuCl}_2(\text{dpan}^{\text{H}})$

	$\text{CuCl}(\text{dpan}^{\text{OMe}})$	$[\text{CuCl}(\text{dpan}^{\text{OMe}})]^+$	$\text{CuCl}_2(\text{dpan}^{\text{H}})$
Cu–N1	2.041(2)	1.980(4)	1.975(3)
Cu \cdots N2	2.527(2)	2.068(4)	2.292(2)
Cu–N3	1.976(2)	2.007(7)	1.979(3)
Cu–Cl	2.253(1)	2.251(2)	2.2869(9)
			2.3109(8)
Cu–O	3.012(2)	2.312(3)	N/A
C \equiv N	1.144(2)	1.136(1)	1.140(1)
τ_5	N/A	0.20	0.43

tighter Cu–N2 bonding interaction are also observed in the Cu–Cl bond lengths, where the Cu–Cl bond distance in $[\text{CuCl}(\text{dpan}^{\text{OMe}})]\text{PF}_6$ is shortened by 0.04 and 0.06 Å relative to the Cu–Cl lengths in $\text{CuCl}_2(\text{dpan}^{\text{H}})$ (Table 1). Structural results from XRD corroborate with the solid-state IR spectra shown in Figure S4 and Table S3. Metallation with Cu(I) results in only minor perturbations to the nitrile stretching frequencies of the uncoordinated ligands. These data provide additional evidence that the Cu(I) ion interacts only minimally with N2 in either ligand framework.

Structural results from the solid state also corroborate with solution-state structural characterization performed by EPR spectroscopy (Figure S5). Here, the solution spectrum of $[\text{CuCl}(\text{dpan}^{\text{OMe}})]\text{PF}_6$ is simulated well with a single axially symmetric species, consistent with the square pyramidal coordination geometry that is experimentally observed (Table S4). Similarly, the EPR spectrum of $\text{CuCl}_2(\text{dpan}^{\text{H}})$ is simulated well with a single rhombic species (Table S5), consistent with the experimentally observed trigonal bipyramidal coordination geometry by XRD (Figure S2).

Electronic Structural Characterization. Ground-state electronic structure investigations were initiated by cyclic voltammetry (CV). The electrochemical properties of the Cu(I) complexes under study exhibit similar properties to those previously investigated.⁷ Tabulated peak potentials are

provided in Table S6, with the corresponding CVs shown in Figure S6. The CuCl(dpan^{OMe}) redox couple is relatively reversible ($i_{pa}/i_{pc} = 1.3$ and $E_a - E_c = 122$ mV, where $E_a - E_c = 146$ mV for Fc⁺⁰) and centered at -377 mV. The CuCl(dpan^H) redox couple is slightly less reversible ($i_{pa}/i_{pc} = 1.4$ and $E_a - E_c = 187$ mV, where $E_a - E_c = 127$ mV for Fc⁺⁰) and centered at -192 mV versus Fc⁺⁰ (Table S6). The decreased reversibility indicated by these data was expected from our understanding of the ground state conformational fluxionality of the Cu(I) complexes under study.⁵

UV-vis absorbance and emission spectra of ligands and Cu(I) complexes are shown in Figure 2, with those of the

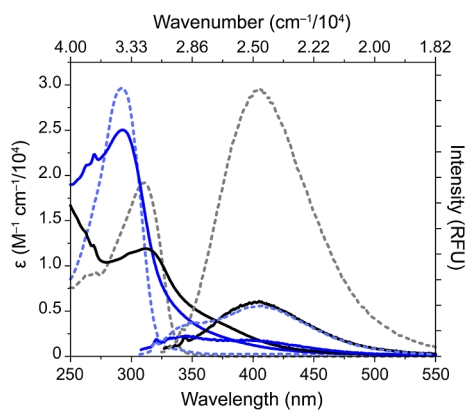


Figure 2. UV-vis absorption and emission spectra of CuCl(dpan^{OMe}) (black solid lines), dpan^{OMe} (gray dashed lines), CuCl(dpan^H) (dark blue solid lines), and dpan^H (light blue dashed lines) in DCM, with $\lambda_{ex} = 310$ and 295 nm for dpan^{OMe} and dpan^H ligands and complexes, respectively.

Cu(II) complexes provided in the Supporting Information. Associated extinction coefficients, absorption and emission maxima, and quantum yields are summarized in Table 2. To enhance our understanding of these spectra, we performed TDDFT calculations of the excited states of the complexes and their ligands.¹⁷ The highest oscillator strength transition in both cases corresponded to the S_5 state from the TDDFT calculation. A natural transition orbital (NTO) analysis was carried out on the highest oscillator strength transitions of the complexes (S_5) and the ligands (S_1) in their optimized ground-state geometries (Figure 3). Here, we find that the absorbance spectra of dpan^{OMe} and dpan^H are dominated by the expected TICT transition, which has $n_N/\pi \rightarrow \pi^*$ character (Figures S7 and S8, respectively). For dpan^H, the LUMO exhibits an

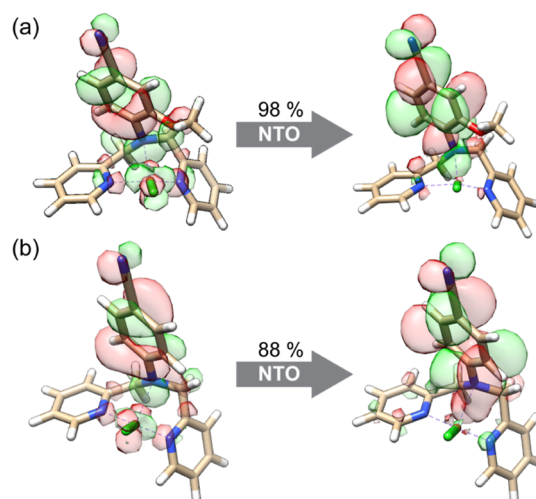


Figure 3. NTOs corresponding to the primary absorption (S_5) derived from TDDFT for CuCl(dpan^{OMe}) (a) and CuCl(dpan^H) (b). Isosurfaces correspond to cutoffs of 0.02.

additional π^* character on the pyridyl arms of the ligand framework (Figure S7). In both cases, the TICT transition comprises $\geq 90\%$ of the total oscillator strength. This result is consistent with the presence of the dialkylaminobenzonitrile fragment, which is structurally related to the best-studied TICT chromophore, dimethylaminobenzonitrile (DMABN).¹⁹ As expected from its likeness to DMABN, dpan^H exhibits dual emission via both TICT and initially formed locally excited (LE) state radiative decay pathways (Figure 2). The addition of the *ortho*-OMe substituent in dpan^{OMe} results in diminished LE emission and only TICT emission is observed in the steady state (Figure 2, Table 2).

The absorption spectra of dpan^H and dpan^{OMe} are only minimally affected by binding to Cu(I). They exhibit lower extinction coefficients and a new shoulder feature/broadening extending toward the visible range (Figure 2, Table 2). Due to these minimal changes, we investigated the NTOs of the dominant absorptions (S_5) in these complexes (with 98 and 88% of the total oscillator strength for CuCl(dpan^{OMe}) and CuCl(dpan^H), respectively) finding that the NTOs consist of a TICT state generated by way of a metal-to-ligand-charge transfer (MLCT, Figure 3). To our knowledge, such an ML-TICT transition has only been reported once before.²⁰ Notably, the NTOs of Figure 3 correspond to the largest oscillators in the UV region (Figure 2). In contrast, the broad shoulder features centered at ~ 375 nm correspond to MLCT

Table 2. Steady-State Absorption and Emission Maxima, Extinction Coefficients, Quantum Yields, and TRPL Lifetimes and Relative Amplitudes^a

	λ_{max} (nm)	ϵ ($M^{-1}cm^{-1}$)	λ_{LE} (nm)	λ_{TICT} (nm)	Φ_F^b	τ_{LE1}^c (ps)	τ_{LE2}^c (ps)	τ_{TICT} (ns) ^c	$k_r, TICT^e$ ($10^6 s^{-1}$)	$k_{nr, TICT}^e$ ($10^8 s^{-1}$)
dpan ^{OMe}	310	19,320		405	0.038(1)	8(1)	60(20)	2.30(4) ^d	16.5(9)	4.18(7)
CuCl(dpan ^{OMe})	313	11,840		405	0.005(1)	9(1)	80(20)	2.30(1)	2.3(3)	4.33(2)
dpan ^H	292	29,630	351	406	0.0071(3)	19(1)	290(80)	0.970(2)	7.4(2)	10.24(2)
CuCl(dpan ^H)	292	25,010	344	400	0.0013(7)	18(1)	180(20)	0.94(1) ^d	1.4(1)	10.6(1)

^aSolutions in DCM had matched O.D. at $\lambda_{ex} = 315$ nm. ^bParenthesis are 1σ from fits obtained according to eq 1. ^cParenthesis are 1σ from fits obtained from averaging fits to data collected on three independently prepared samples. ^dThese two data sets were only assessed in duplicate. Kinetics assessments were performed by averaging photons detected over $\lambda_{det} = 350$ – 370 nm for LE*, and $\lambda_{det} = 415$ – 435 nm for TICT* and fitting to a two- (LE) or one- (TICT) component sum of exponentials convoluted with a Gaussian instrument response function. ^eRadiative and nonradiative rate constants k_r and k_{nr} obtained from imposing the simplification that 100% of Φ_F originates from the TICT* state, when in reality it ranges from 91 to 96%.

transitions in which the acceptor orbital is localized on the pyridyl arms of the ligands. In our time-resolved spectroscopic studies (vide infra), we excite at 315 nm, likely giving rise to both types of transitions. However, we have previously shown that control experiments with TICT-inactive $\text{CuCl}(\text{dpa}^{\text{R}})$ complexes ($\text{R} = \text{H}$ and OMe) produce excited states that exist only fleetingly and are $\sim 10^3$ -fold shorter lived than the excited state lifetimes under investigation here arising from the ML-TICT transition.⁷

Comparative emission spectra of ligands and complexes are presented in Figure 2. dpan^{OMe} exhibits only one emission feature that is consistent in energy and lifetime (vide infra) with emission from a TICT excited state, while dpan^{H} exhibits dual emission, consistent with emission from both LE and TICT states. The lower intensity of emission from the $\text{Cu}(\text{I})$ complexes relative to their corresponding uncoordinated ligand is reflected in the quantum yields (Φ_{F}) listed in Table 2. Φ_{F} decreases ~ 7 -fold for both complexes relative to their uncoordinated ligands. In previous studies with dpaa^{R} ligands featuring an acyl electron-withdrawing group instead of a nitrile, we observed a similar phenomenon with $\text{R} = \text{OMe}$. However, for $\text{R} = \text{H}$, Φ_{F} was relatively unaffected by the presence of $\text{Cu}(\text{I})$.⁷ In those systems, dpaa^{H} emits primarily ($\sim 85\%$) from the LE state while dpaa^{OMe} emits primarily ($\sim 95\%$) from the TICT state. Combined with the current results, these cumulative data suggest that emission quenching in the presence of $\text{Cu}(\text{I})$ is facilitated by TICT-active ligands.

Time-Resolved Photoluminescence (TRPL) Spectroscopy. To gain insight into the excited state decay pathways operative in these complexes, LE and TICT emission lifetimes (τ_{LE} and τ_{TICT} , respectively) of dpan^{OMe} , dpan^{H} , and their corresponding $\text{Cu}(\text{I})$ complexes were measured by TRPL spectroscopy. The results of these studies are summarized in Table 2 and exemplary data are presented in Figures S9–S10. All samples were excited at 315 nm, and photons counted over a spectral range of 250–740 nm. Time ranges of 0–120 ps and 0–50 ns were selected to assess LE and TICT excited state decay processes, respectively. Unlike what we observe in the steady state, time resolution reveals that a discrete LE state does exist for dpan^{OMe} and $\text{CuCl}(\text{dpan}^{\text{OMe}})$. The kinetics of TICT decay were analyzed by averaging photons detected on the 50 ns timescale over 415–435 nm and fitting to a monoexponential decay. LE kinetics were assessed by averaging photons detected on the 120 ps timescale over 350–370 nm and fitting to a biexponential decay. In all cases, the relative amplitudes of these decay traces at $t = 0$ reveal that $>85\%$ of emission intensity originates from the TICT state (Figures S9–S10).

Lifetimes of TICT emission range from ~ 1 to 2 ns across this series, consistent with literature reports of nitrile-based TICT fluorophores.^{21–23} Lifetimes of LE emission required a biexponential fit to accurately encapsulate relaxation to the ground state (τ_{LE1}), and decay into the TICT state (τ_{LE2}). Consistent with the literature on DMABN, τ_{LE1} arising from decay to ground range from ~ 10 to 20 ps, while τ_{LE2} arising from decay to the TICT state range from ~ 60 to 300 ps. Combining the TICT lifetimes measured by TRPL spectroscopy, and the Φ_{F} measured in the steady state, we are able to approximate radiative and nonradiative contributions to the observed TICT lifetimes (k_{r} and k_{nr} in Table 2), where this analysis requires that we assume (incorrectly) that 100% of Φ_{F} originates from a TICT state. This approximation inherently incurs a 5–10% error based on an analysis of the relative

amplitudes of TICT and LE signals at the start of the 50 ns and 120 ps timescale measurements, respectively. Notwithstanding, the approximation is useful in understanding the photophysical processes at play in these dual emissive systems. We find that k_{nr} are identical for each set of ligand/complex and that differences in Φ_{F} result purely from differences in k_{r} (Table 2).⁷

TA Spectroscopy. To gain further insight into the excited state processes at play we performed fs TA spectroscopy. Spectral traces observed for dpan^{OMe} and $\text{CuCl}(\text{dpan}^{\text{OMe}})$ are provided in Figure 4, while the spectral traces observed for

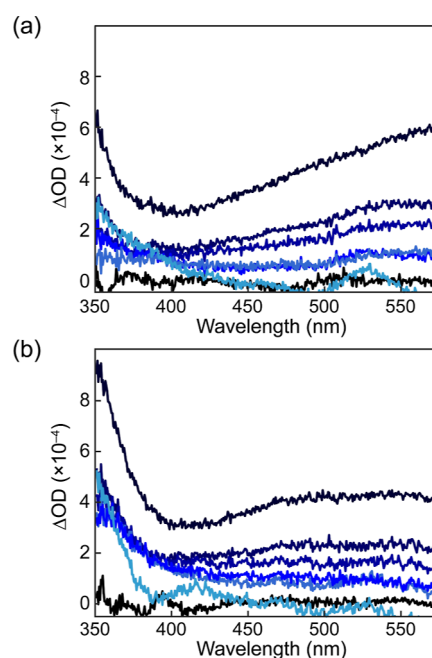


Figure 4. TA spectra collected at -1 , 5 , 50 , 100 , 250 , 500 , and 3000 ps (dark to light) upon excitation of dpan^{OMe} (a) and $\text{CuCl}(\text{dpan}^{\text{OMe}})$ (b) at $\lambda_{\text{ex}} = 315$ nm in DCM.

$\text{CuCl}(\text{dpan}^{\text{H}})$ are provided in Figure S11. All three samples exhibit similar excited state absorbance (ESA) features to that of the well-studied TICT fluorophore, DMABN.^{22–24} On the timescale of our experiments (to 3 ns) the spectra primarily feature $S_1 \rightarrow S_n$ transitions exhibiting a sharp feature centered at ~ 350 nm and a broad feature spanning the region >400 nm. At late time points, evidence for the expected $T_1 \rightarrow T_n$ transitions can be seen in the higher energy region (lightest blue traces in Figure 4).²⁵ The line shapes for ligand versus metal complex differ slightly, but kinetics analyses (Figure S12) reveal that similar processes are operative in the presence and absence of metal. As shown in Table 3, fitting these data to a triexponential function to encapsulate the LE decay to ground

Table 3. Excited State Lifetimes from TA Spectroscopy^a

	τ_1 (ps)	τ_2 (ps)	τ_3 (ns)
dpan^{OMe}	10(3)	90(20)	1.5(2)
$\text{CuCl}(\text{dpan}^{\text{OMe}})$	11(5)	100(40)	2.0(3)
$\text{CuCl}(\text{dpan}^{\text{H}})$	8(2)	90(10)	2.4(3)

^aLifetimes were obtained by fitting spectral slices taken at 500 nm for dpan^{OMe} , 490 nm for $\text{CuCl}(\text{dpan}^{\text{OMe}})$, and 475 nm for $\text{CuCl}(\text{dpan}^{\text{H}})$ to a sum of exponentials convoluted with a Gaussian instrument response function. Parentheses represent 1σ relative to the fit.

state, LE decay to TICT, and TICT decay, produces lifetimes that are consistent with our kinetics assessments by TRPL spectroscopy. Nearly identical values were obtained by fitting the TA decay across a range of wavelengths in the visible region, suggesting that all three lifetimes arise from excited states with spectral overlap (Figure S13). Gratifyingly, we observe <5% sample degradation for both metal complexes (as assessed by UV–vis abs spectroscopy, Table S1) under photochemical conditions (i.e., after $\sim 3.3 \times 10^6$ laser shots at 500 μW power). This stability may result directly from the ability of dpan^R ligands to accommodate the conformational changes inherent to Cu(II/I) redox chemistry.²⁶

Excited State Geometry Optimization. Intrigued by our NTO analyses that predict the generation of a TICT state via MLCT, we performed excited state geometry optimizations to compute a predicted molecular structure upon photoexcitation. In performing excited state optimizations, we make the assumption that the excitation to the highest absorbing state of the complexes (S_5) rapidly relaxes to the lowest lying excited state (S_1), and thus perform excited state geometry optimizations using the S_1 states. The results of these calculations are depicted in Figures 5 and S14, with select bond distances and angles listed in Tables 4 and S7.

Table 4. Select Bond Lengths (Å) and Angles (°) from Ground and Excited State Geometry Optimizations^a

	Cu...N2	Cu...O	N2...Cu...Cl	torsion angle ^b
CuCl(dpan ^{OMe})	2.554	2.961	139.2	54.4
[CuCl(dpan ^{OMe})] ⁺	2.090	2.468	171.3	39.2
[CuCl(dpan ^{OMe})] [*]	2.153	2.541	170.6	41.9

^awB97X-D3/def2-TZVP/SMD DFT and TDDFT geometry optimizations of the S_0 , S_0^+ , and S_1 electronic states. Corresponding geometries provided in Supporting Information. ^bDefined as the angle formed between the Cu–N2 vector and the plane of the phenyl ring.

Experimentally, we observe that the coordination geometries of Cu(I) and Cu(II) within the dpan^R ligand scaffold are distinct from one another (Figure 1). This result is also reproduced computationally. The geometry-optimized structures of CuCl(dpan^{OMe}) and [CuCl(dpan^{OMe})]⁺ also support that significant rearrangements take place upon oxidation of the neutral Cu(I) complexes (bottom row in Figure 5). Performing geometry optimizations on the lowest energy (S_1) excited states, we found that they converge to a coordination environment that is strikingly similar to the ground state Cu(II) structures (top row in Figure 5). Of particular note are the Cu–N2 bond distances, which serve as a key metric for the detection of Cu(II) character and contract by ~ 0.4 Å upon oxidation (Tables 1 and 4). The similarities between [CuCl(dpan^{OMe})]⁺ and [CuCl(dpan^{OMe})]^{*} are not reproduced for [CuCl(dpan^H)]⁺ and [CuCl(dpan^H)]^{*} (Figure S14 and Table S7). These observations lend credence to our ligand design strategy, wherein the *ortho*-OMe substituent serves as a key component capable of locking in a transiently formed Cu(II) species. The results presented here are also consistent with our prediction that the photogenerated TICT state forms by way of MLCT and provide precedence for our strategy of using phototriggered structural rearrangements to engender control over the formation and decay of a CS state.

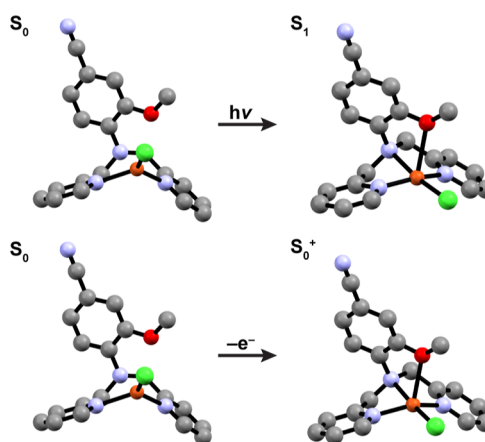


Figure 5. Ground (S_0 and S_0^+) and excited (S_1) state geometry optimized structures of [CuCl(dpan^{OMe})]^{+/0/*} highlighting the similarities between the Cu(II) coordination environment (S_0^+) and that formed in the excited state (S_1).

DISCUSSION AND CONCLUSIONS

Ground state structural and solution characterization of CuCl(dpan^{OMe}) supports that we have successfully prepared a coordination complex capable of stabilizing Cu(I) and Cu(II) in distinct coordination geometries and environments. Investigating the UV–vis absorption and emission properties of the dpan^{OMe} ligand and its complex with Cu(I) reveals that an unusual MLCT-generated TICT state comprises the primary (98%) oscillator in the Cu(I) complex. Surprisingly, we do not see the redshift in the absorption spectra of these complexes that would normally be expected for an MLCT transition. A previously published report from Meneghetti et al. reveals a similar phenomenon in a series of ferrocene-functionalized acceptor molecules that also have orthogonal HOMO and LUMO orbitals, suggesting that this aspect may be relevant.²⁰

Emission from the Cu(I) complexes under study is quenched relative to emission from the ligands alone. Combined with analyses from TRPL spectroscopy, we are able to attribute the decreased Φ_F of the complexes relative to their uncoordinated ligands to decreases in k_r . In our previous work, we observed a similar phenomenon in the case of the TICT-active dpaa^{OMe} ligand and complex. However, in those studies, we did not observe quenching of dpaa^H ligand emission in the presence of Cu(I). The dpaa^H ligand is only weakly TICT emissive, while in the present study, dpan^H is strongly TICT emissive. Together, these findings indicate that modulation of k_r occurs via a metal-functionalized TICT excited state. This result may have implications in the design of new molecules and materials for which manipulation of k_r represents a key strategy toward achieving high luminosity.

The photophysics of dpaa^R ligands and complexes explored previously were dominated by undesirable ligand-centered excited state transitions. The TA spectra exhibited intense ESAs consistent with acyl-mediated $\pi \rightarrow \pi^*$ and $n_O \rightarrow \pi^*$ transitions, where vibrational coupling of the acyl group with the aromatic ring allowed easy access to these unwanted excited states.^{7,27,28} We reasoned that by changing the acyl group to a nitrile group, the associated vibrational states would be energetically mismatched for efficient coupling to the aromatic ring.²⁷ Gratifyingly, we found that this modification greatly simplifies the TA spectra (Figure 4). We are now able

to describe the photophysics in these systems with a simple Jablonski diagram (Figure 6) relevant to many TICT

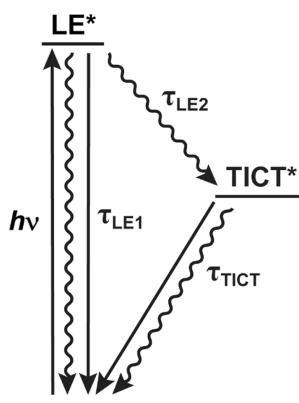


Figure 6. The Jablonski diagram established for TICT fluorophores is in good agreement with our observations by TA and TRPL spectroscopies in which three lifetimes are observed.

fluorophores in which excitation produces dual emissive states (LE and TICT). We observe both of these states by TRPL and can measure the conversion of LE to TICT, producing lifetimes that are consistent with previous reports on related DMABN molecules.^{25,29–32}

The energies of TICT emission remain essentially unchanged upon complexation with Cu(I) (Table 2). This observation is in line with the XRD data listed in Table 1; the interaction between N2 and the Cu ion is weak. We have previously shown that this weak interaction enables dynamicity among this family of complexes in solution.^{5,6} Similarly here, if the interactions between N2 and Cu(I) were strong, we might expect to see more substantial shifts in TICT emission upon metallation.^{33,34} Perhaps for these reasons, our analyses of the TRPL data on these ligands and complexes reveal that the lifetimes of LE and TICT emission, and the rates of conversion of the former to the latter, agree well with those reported for DMABN and related organic compounds.^{22,35,36} According to all of these findings, it was a surprise to us that excited state geometry optimization of the two Cu(I) complexes support the formation of a transient CS state. However, given the unique structural signatures of the two oxidation states, our computational results are clear. Contrasted with the equally unambiguous spectroscopic results suggesting that the presence of Cu(I) has little effect on the excited state lifetimes of the ligand fluorophores, the findings reported here pose a thought-provoking paradigm. Having recently determined the inner sphere reorganization energies associated with the Cu(II/I) self-exchange reactions among this family of complexes in the dark,³⁷ we are poised to investigate the effects of driving force modifications on CS lifetimes. Our work is set for future studies.

■ ASSOCIATED CONTENT

Supporting Information

The Supporting Information is available free of charge at <https://pubs.acs.org/doi/10.1021/acs.jpca.3c04269>.

Ligand synthesis, XRD structures (CCDC 2272135–2272139) and refinement parameters, NMR and IR spectra, EPR spectra, simulations, and parameters, CVs and midpoint potentials, NTO analyses and additional

excited state geometry optimizations, exemplary TRPL data and fits, TA heatmaps and exemplary fits (PDF)

■ AUTHOR INFORMATION

Corresponding Author

Lisa Olshansky – University of Illinois, Urbana-Champaign, Urbana, Illinois 61801, United States; orcid.org/0000-0003-1076-9318; Email: lolshans@illinois.edu

Authors

Bronte J. Charette – University of Illinois, Urbana-Champaign, Urbana, Illinois 61801, United States
 Shelby R. King – University of Illinois, Urbana-Champaign, Urbana, Illinois 61801, United States
 Jiaqi Chen – University of Illinois, Urbana-Champaign, Urbana, Illinois 61801, United States; orcid.org/0000-0001-8237-7773
 Annika R. Holm – University of Illinois, Urbana-Champaign, Urbana, Illinois 61801, United States
 Justin T. Malme – University of Illinois, Urbana-Champaign, Urbana, Illinois 61801, United States
 Robert D. Cook – University of Illinois, Urbana-Champaign, Urbana, Illinois 61801, United States
 Richard D. Schaller – Center for Nanoscale Materials, Argonne National Laboratory, Lemont, Illinois 60439, United States
 Nicholas E. Jackson – University of Illinois, Urbana-Champaign, Urbana, Illinois 61801, United States; orcid.org/0000-0002-1470-1903

Complete contact information is available at: <https://pubs.acs.org/10.1021/acs.jpca.3c04269>

Notes

The authors declare no competing financial interest.

■ ACKNOWLEDGMENTS

B.J.C. gratefully acknowledges the University of Illinois' Office of the Vice Chancellor for Diversity, Equity & Inclusion for the Illinois Distinguished Postdoctoral Fellowship. A.R.H. acknowledges the NSF GRFP, and R.D.C. acknowledges the 3M Corporation for the C² Summer Research Scholarship. This work was performed, in part, at the Center for Nanoscale Materials, a U.S. Department of Energy Office of Science User Facility, and supported by the U.S. Department of Energy, Office of Science, under Contract no. DE-AC02-06CH11357. L.O. gratefully acknowledges support from the U.S. Department of Energy, Office of Science, Basic Energy Sciences under Award #DE-SC0022846.

■ REFERENCES

- (1) Efremov, R. G.; Sazanov, L. A. Respiratory Complex I: 'Steam Engine' of the Cell. *Curr. Opin. Struct. Biol.* **2011**, *21*, 532–540.
- (2) Shlyk, O.; Samish, I.; Matěnová, M.; Dulebo, A.; Poláková, H.; Kaftan, D.; Scherz, A. A Single Residue Controls Electron Transfer Gating in Photosynthetic Reaction Centers. *Sci. Rep.* **2017**, *7*, No. e44580.
- (3) Davidson, V. L. Protein Control of True, Gated, and Coupled Electron Transfer Reactions. *Acc. Chem. Res.* **2008**, *41*, 730–738.
- (4) Danyal, K.; Mayweather, D.; Dean, D. R.; Seefeldt, L. C.; Hoffman, B. M. Conformational Gating of Electron Transfer from the Nitrogenase Fe Protein to MoFe Protein. *J. Am. Chem. Soc.* **2010**, *132*, 6894–6895.

- (5) Charette, B. J.; Griffin, P. J.; Zimmerman, C. M.; Olshansky, L. Conformationally Dynamic Copper Coordination Complexes. *Dalton Trans.* **2022**, *51*, 6212–6219.
- (6) Griffin, P. J.; Dake, M. J.; Remolina, A. D.; Olshansky, L. Conformational Dynamicity in a Copper(II) Coordination Complex. *Dalton Trans.* **2023**, *52*, 8376–8383.
- (7) Griffin, P. J.; Charette, B. J.; Burke, J. H.; Vura-Weis, J.; Schaller, R. D.; Gosztola, D. J.; Olshansky, L. Toward Improved Charge Separation through Conformational Control in Copper Coordination Complexes. *J. Am. Chem. Soc.* **2022**, *144*, 12116–12126.
- (8) Conry, R. R. Copper: Inorganic & Coordination Chemistry Based in Part on the Article Copper: Inorganic & Coordination Chemistry by Rebecca R. Conry & Kenneth D. Karlin Which Appeared in the Encyclopedia of Inorganic Chemistry. In *Encyclopedia of Inorganic Chemistry*, 1st ed.; Wiley Online Library, 2005.
- (9) Dey, N.; Kumari, N.; Biswakarma, D.; Jha, S.; Bhattacharya, S. Colorimetric Indicators for Specific Recognition of Cu²⁺ and Hg²⁺ in Physiological Media: Effect of Variations of Signaling Unit on Optical Response. *Inorg. Chim. Acta.* **2019**, *487*, 50–57.
- (10) Gwizdala, C.; Singh, C. V.; Friss, T. R.; Macdonald, J. C.; Burdette, S. C. Quantifying Factors That Influence Metal Ion Release in Photocaged Complexes Using ZinCast Derivatives. *Dalton Trans.* **2012**, *41*, 8162–8174.
- (11) Stoll, S.; Schweiger, A. EasySpin, a Comprehensive Software Package for Spectral Simulation and Analysis in EPR. *J. Magn. Reson.* **2006**, *178*, 42–55.
- (12) Heinrich, G.; Schoof, S.; Gusten, H. 9,10-Diphenylanthracene as a Fluorescence Quantum Yield Standard. *J. Photochem.* **1974**, *3*, 315–320.
- (13) Morris, J. V.; Mahaney, M. A.; Huber, J. R. Fluorescence Quantum Yield Determinations. 9,10-Diphenylanthracene as a Reference Standard in Different Solvents. *J. Phys. Chem.* **1976**, *80*, 969–974.
- (14) Sheldrick, G. M. Crystal Structure Refinement with SHELXL. *Acta Crystallogr., Sect. C: Struct. Chem.* **2015**, *71*, 3–8.
- (15) Sheldrick, G. M. SHELXT—Integrated Space-Group and Crystal-Structure Determination. *Acta Crystallogr., Sect. A: Found. Adv.* **2015**, *71*, 3–8.
- (16) Dolomanov, O. V.; Bourhis, L. J.; Gildea, R. J.; Howard, J. A. K.; Puschmann, H. OLEX2 : A Complete Structure Solution, Refinement and Analysis Program. *J. Appl. Crystallogr.* **2009**, *42*, 339–341.
- (17) Neese, F. Software Update: The ORCA Program System—Version 5.0. *Wiley Interdiscip. Rev.: Comput. Mol. Sci.* **2022**, *12*, No. e1606.
- (18) Addison, A. W.; Rao, T. N.; Reedijk, J.; van Rijn, J.; Verschoor, G. C. Synthesis, Structure, and Spectroscopic Properties of Copper(II) Compounds Containing Nitrogen–Sulphur Donor Ligands; the Crystal and Molecular Structure of Aqua[1,7-Bis(N-Methylbenzimidazol-2'-yl)-2,6-Dithiaheptane]Copper(II) Perchlorate. *J. Chem. Soc., Dalton Trans.* **1984**, *7*, 1349–1356.
- (19) Grabowski, Z. R.; Rotkiewicz, K.; Rettig, W. Structural Changes Accompanying Intramolecular Electron Transfer: Focus on Twisted Intramolecular Charge-Transfer States and Structures. *Chem. Rev.* **2003**, *34*, 3899–4032.
- (20) Scuppa, S.; Orian, L.; Donoli, A.; Santi, S.; Meneghetti, M. Anti-Kasha's Rule Fluorescence Emission in (2-Ferrocenyl)Indene Generated by a Twisted Intramolecular Charge-Transfer (TICT) Process. *J. Phys. Chem. A* **2011**, *115*, 8344–8349.
- (21) Schuddeboom, W.; Jonker, S. A.; Warman, J. M.; Leinhos, U.; Kuehnle, W.; Zachariasse, K. A. Excited-State Dipole Moments of Dual Fluorescent 4-(Dialkylamino)Benzonitriles: Influence of Alkyl Chain Length and Effective Solvent Polarity. *J. Phys. Chem.* **1992**, *96*, 10809–10819.
- (22) Druzhinin, S. I.; Ernsting, N. P.; Kovalenko, S. A.; Lustres, L. P.; Senyushkina, T. A.; Zachariasse, K. A. Dynamics of Ultrafast Intramolecular Charge Transfer with 4-(Dimethylamino)Benzonitrile in Acetonitrile. *J. Phys. Chem. A* **2006**, *110*, 2955–2969.
- (23) Volchkov, V. V.; Khimich, M. N.; Rusalov, M. V.; Gostev, F. E.; Shelaev, I. V.; Nadochenko, V. A.; Gromov, S. P.; Melnikov, M. Ya. Intramolecular Photo-driven Electron Transfer in the Series of DMABN Related Compounds with Para-substituted Acceptors. Study of the Rate Constants by Marcus Theory. *J. Phys. Org. Chem.* **2020**, *33*, No. e4041.
- (24) Kochman, M. A.; Durbeej, B.; Kubas, A. Simulation and Analysis of the Transient Absorption Spectrum of 4-(N,N-Dimethylamino)Benzonitrile (DMABN) in Acetonitrile. *J. Phys. Chem. A* **2021**, *125*, 8635–8648.
- (25) Okada, T.; Uesugi, M.; Köhler, G.; Rechthaler, K.; Rotkiewicz, K.; Rettig, W.; Grabner, G. Time-Resolved Spectroscopy of DMABN and Its Cage Derivatives 6-Cyanobenzquinuclidine (CBQ) and Benzquinuclidine (BQ). *Chem. Phys.* **1999**, *241*, 327–337.
- (26) Gimeno, L.; Phelan, B. T.; Sprague-Klein, E. A.; Roisnel, T.; Blart, E.; Gourlaouen, C.; Chen, L. X.; Pellegrin, Y. Bulky and Stable Copper(I)-Phenanthroline Complex: Impact of Steric Strain and Symmetry on the Excited-State Properties. *Inorg. Chem.* **2022**, *61*, 7296–7307.
- (27) Chan, C. T.-L.; Ma, C.; Chan, R. C.-T.; Ou, H.-M.; Xie, H.-X.; Wong, A. K.-W.; Wang, M.-L.; Kwok, W.-M. A Long Lasting Sunscreen Controversy of 4-Aminobenzoic Acid and 4-Dimethylaminobenzaldehyde Derivatives Resolved by Ultrafast Spectroscopy Combined with Density Functional Theoretical Study. *Phys. Chem. Chem. Phys.* **2020**, *22*, 8006–8020.
- (28) Fujiwara, T.; Lee, J. K.; Zgierski, M. Z.; Lim, E. C. Intramolecular Charge Transfer in the Excited State of 4-Dimethylaminobenzaldehyde and 4-Dimethylaminoacetophenone. *Chem. Phys. Lett.* **2009**, *481*, 78–82.
- (29) Okada, T.; Mataga, N.; Baumann, W. S_n ← S₁ Absorption Spectra of 4-(N,N-Dimethylamino)Benzonitrile in Various Solvents: Confirmation of the Intramolecular Ion Pair State in Polar Solvent. *J. Phys. Chem.* **1987**, *91*, 760–762.
- (30) Chutny, B.; Swallow, A. J. Aromatic Anions and Free Radicals in the Pulse Radiolysis of Aqueous Solutions of Benzonitrile. *Trans. Faraday Soc.* **1970**, *66*, 2847–2854.
- (31) Shida, T.; Iwata, S.; Imamura, M. Electronic Absorption Spectra of Ion Radicals and Their Molecular Orbital Interpretation. IV. Anion Radicals of Aromatic and Unsaturated Aliphatic Carbonyl Compounds. *J. Phys. Chem.* **1974**, *78*, 741–748.
- (32) Ishitani, A.; Nagakura, S. The Electronic Spectra of the Anion Radicals of Substituted Benzenes. *Theor. Chim. Acta* **1966**, *4*, 236–249.
- (33) Chaudhry, A. F.; Verma, M.; Morgan, M. T.; Henary, M. M.; Siegel, N.; Hales, J. M.; Perry, J. W.; Fahrni, C. J. Kinetically Controlled Photoinduced Electron Transfer Switching in Cu(I)-Responsive Fluorescent Probes. *J. Am. Chem. Soc.* **2010**, *132*, 737–747.
- (34) Aoki, S.; Kagata, D.; Shiro, M.; Takeda, K.; Kimura, E. Metal Chelation-Controlled Twisted Intramolecular Charge Transfer and Its Application to Fluorescent Sensing of Metal Ions and Anions. *J. Am. Chem. Soc.* **2004**, *126*, 13377–13390.
- (35) Changenet, P.; Plaza, P.; Martin, M. M.; Meyer, Y. H. Role of Intramolecular Torsion and Solvent Dynamics in the Charge-Transfer Kinetics in Triphenylphosphine Oxide Derivatives and DMABN. *J. Phys. Chem. A* **1997**, *101*, 8186–8194.
- (36) Park, M.; Kim, C. H.; Joo, T. Multifaceted Ultrafast Intramolecular Charge Transfer Dynamics of 4-(Dimethylamino)-Benzonitrile (DMABN). *J. Phys. Chem. A* **2013**, *117*, 370–377.
- (37) Griffin, P. J.; Olshansky, L. Rapid Electron Transfer Self-Exchange in Conformationally Dynamic Copper Coordination Complexes. *J. Am. Chem. Soc.* **2023**, just accepted.